coatings

MDPI

Article

Regulations of Thermal Expansion Coefficients of $Yb_{1-x}Al_xTaO_4$ for Environmental Barrier Coatings Applications

Jiaxin Liao, Lin Chen *, Luyang Zhang, Xunlei Chen, Cheng Xu, Tianyu Li and Jing Feng *

Faculty of Materials Science and Engineering, Kunming University of Science and Technology, Kunming 650093, China; ljx09101999@163.com (J.L.); 17787877884@163.com (L.Z.); chenxunlei0406@163.com (X.C.); xucheng9898@163.com (C.X.); m18798493126_2@163.com (T.L.)

* Correspondence: ceramicscl@163.com (L.C.); jingfeng@kust.edu.cn (J.F.); Tel.: +86-18288268680 (L.C.); +86-15925200330 (J.F.)

Abstract: Environmental barrier coatings (EBCs) are widely used to protect ceramic matrix composites (CMCs, SiC_f/SiC, and Al_2O_{3f}/Al_2O_3), and they should have low thermal expansion coefficients (TECs) matching the CMCs and excellent mechanical properties to prolong their lifetime. Current EBC materials have disadvantages of phase transitions and insufficient mechanical properties, which affect their working temperatures and lifetime. It is necessary to develop new oxide EBCs. Ytterbium tantalate ($YbTaO_4$) is a stable and novel EBC material, and we have improved the mechanical properties and TECs of $Yb_{1-x}Al_xTaO_4$ (x = 0.05, 0.1, 0.2, 0.3, 0.4, 0.5) ceramics by replacing Yb with Al. XRD, SEM, and EDS are used to verify the crystal and microstructures, and nano-indentation is used to measure the modulus and hardness when changes in TECs are measured within a thermal expansion device. The results show that the phase structure of $Yb_{1-x}Al_xTaO_4$ (x = 0.05, 0.1, 0.2, 0.3, 0.4, 0.5) is stable at 25–1400 °C within air atmosphere, and their high-temperature TECs (6.4–8.9 × 10^{-6} K^{-1}, 1400 °C) are effectively regulated by introductions of different contents of Al, which enlarge their engineering applications for SiC_f/SiC and Al_2O_{3f}/Al_2O_3 CMCs. The evolutions of TECs are analyzed from structural characteristics and phase compositions, and the increased TECs make $Yb_{1-x}Al_xTaO_4$ potential EBCs for Al_2O_3 matrixes. Due to the high bonding strength of Al–O bonds, hardness, as well as Young's modulus, are enhanced with the increasing Al content, with $Yb_{1-x}Al_xTaO_4$ (x = 0.05, 0.1, 0.2, 0.3, 0.4, 0.5) having a nano-hardness of 3.7–12.8 GPa and a Young's modulus of 100.9–236.6 GPa. The TECs of $YbTaO_4$ are successfully regulated to expand their applications, and they match those of Al_2O_3 and SiC matrixes, as well as displaying improved mechanical properties. This work promotes applications of $YbTaO_4$ as potential EBCs and provides a new way to regulate the TECs of tantalates.

Keywords: environmental barrier coatings; rare-earth tantalates; thermal expansion coefficients; mechanical properties; nano-indentation

check for updates

Citation: Liao, J.; Chen, L.; Zhang, L.; Chen, X.; Xu, C.; Li, T.; Feng, J. Regulations of Thermal Expansion Coefficients of $Yb_{1-x}Al_xTaO_4$ for Environmental Barrier Coatings Applications. *Coatings* **2024**, *14*, 1097. https://doi.org/10.3390/coatings14091097

Academic Editors: Luka Pavic and Jana Pisk

Received: 30 July 2024
Revised: 22 August 2024
Accepted: 22 August 2024
Published: 31 August 2024

Copyright: © 2024 by the authors. Licensee MDPI, Basel, Switzerland. This article is an open access article distributed under the terms and conditions of the Creative Commons Attribution (CC BY) license (https://creativecommons.org/licenses/by/4.0/).

1. Introduction

Currently, high-temperature nickel-based alloys are the primary materials used as hot-end components of aviation engines. With the rapid advancement of aircraft components and the increases in the power of engines, the maximum working temperature (1150 °C) of nickel-based alloys cannot meet their requirements. Thermal barrier coatings (TBCs) are applied to the surface of nickel-based components to provide thermal insulation accompanied with cooling technologies, which increase working temperatures [1–3]. However, the effects of TBCs are limited, and the traditional zirconate-based TBCs have working temperatures of less than 1200 °C [4]. Additionally, alloys have a high density, which increases the overall weight of engines to reduce fuel efficiency.

Accordingly, lightweight high-temperature ceramic matrix composites (CMCs) with operating temperatures of 1000–1650 °C are noticed for their outstanding performances [5–9]. Using CMCs can reduce the weight of these components and significantly enhance the thrust-to-weight ratio [10]. Common CMCs include Al_2O_3, C, and SiC fiber-reinforced Al_2O_3, as

well as C fiber-toughened SiC (C_f/SiC) and SiC fiber-reinforced SiC (SiC_f/SiC) [11–13]. CMCs are susceptible to corrosion by molten salts, oxygen, and steam at high temperatures, which significantly reduce their lifespan [14–18]. Based on the above situations, environmental barrier coatings (EBCs) are mostly applied to shield CMCs from damages caused by high-temperature steam and oxygen, thereby extending their service life [19–21]. Oxide EBCs should have low thermal expansion coefficients (TECs, 3~9 $\times$ 10^{-6} K^{-1}) to match those of CMCs, and the interface thermal stress should be reduced as much as possible. The main functions of EBCs are isolating high-temperature steam and oxides to avoid the premature failure of CMCs; thus, EBCs must be stable at high temperatures. It can be seen that excellent high-temperature stability, adjustable TECs, and outstanding mechanical properties are essential for novel EBC materials.

The first-generation EBCs are mullite, which has low TECs and outstanding chemical compatibility with SiC. However, mullite will produce cracks during thermal cycling [22]. By combining mullite with yttria-stabilized zirconia (YSZ), researchers have improved the properties of mullite. YSZ has high TECs, which lead to thermal stress, and the resultant cracks allow water vapor to penetrate through EBCs to corrode CMCs [23,24]. Barium strontium aluminosilicate (BSAS) shows a substantial improvement in performance, but its high-temperature volatility and poor chemical compatibility with SiO_2 limit its applications [25]. Rare earth silicates (Rare earth = RE, RE_2SiO_5, and $RE_2Si_2O_7$) with low TECs and excellent SiO_2 chemical compatibility have replaced previous EBCs [26,27]. RE_2SiO_5 can withstand high temperatures for extended periods; however, they are unstable at temperatures beyond 1200 °C, and the phase transformations between polymorphs can produce strain and cracks which cause failure. It can be seen that excellent high-temperature stability is essential for EBCs. Additionally, the TECs of CMCs span from about 3 $\times$ 10^{-6} K^{-1} to 9 $\times$ 10^{-6} K^{-1} [17,28–32], indicating that low TECs are necessary for EBCs.

Chen et al. [33,34] have reported that $YbTaO_4$ and $AlTaO_4$ are stable without phase changes at 25~1500 °C, and they show excellent chemical compatibility with SiO_2. At 1200 °C, the TECs of $YbTaO_4$ and $AlTaO_4$ are 7.6 $\times$ 10^{-6} K^{-1} and 5.6 $\times$ 10^{-6} K^{-1}, respectively. The above characteristics suggest that $YbTaO_4$ and $AlTaO_4$ are novel oxide EBCs. $YbTaO_4$ has weaknesses of a relatively low modulus and low hardness, which are not beneficial for its EBC applications. It is necessary to optimize the properties of $YbTaO_4$ EBCs, including TECs and mechanical properties. To expand the engineering applications of $YbTaO_4$, we adjust its TECs by Al-substituted Yb to form $Yb_{1-x}Al_xTaO_4$ (x = 0.05, 0.1, 0.2, 0.3, 0.4, 0.5) oxides. $AlTaO_4$ has a higher hardness and modulus than $YbTaO_4$, and Al-substituting Yb can enhance the mechanical properties of $YbTaO_4$ [35,36]. The results indicate that $Yb_{1-x}Al_xTaO_4$ ceramics have TECs matching SiC_f/SiC and Al_2O_{3f}/Al_2O_3 CMCs, and their TECs are successfully regulated by Al substitution. Furthermore, the hardness and modulus of $YbTaO_4$ are simultaneously enhanced to improve their lifetime. In a future study, it is necessary to research the CaO-MgO-$AlO_{1.5}$-SiO_2 corrosion and oxidation resistance properties of $YbTaO_4$. Overall, $Yb_{1-x}Al_xTaO_4$ ceramics have significant potential as EBCs according to their adjustable TECs and improved mechanical properties.

2. Experiments

2.1. Sample Synthesis

The synthesis of $Yb_{1-x}Al_xTaO_4$ samples (x = 0.05, 0.1, 0.2, 0.3, 0.4, 0.5) used Yb_2O_3 (purity $\geq$ 99.99%), Al_2O_3 (purity $\geq$ 99.99%), and Ta_2O_5 (purity $\geq$ 99.99%) powders from Aladdin, China, and their particle sizes were less than 10 μm. The raw powders were maintained at 1000 °C for 3 h to remove any moisture and then were mixed based on their chemical formula. Anhydrous ethanol was mixed with the weighted powders, and the mixtures were ball-milled for 12 h at 300 rpm. The mixed powders were dried at 100 °C for 12 h. The powders were subsequently pressed under a pressure of 6 MPa for 2 min to obtain ceramic disks. Finally, the disks were sintered at 1500~1700 °C in atmospheric conditions for 3–6 h to produce dense $Yb_{1-x}Al_xTaO_4$ ceramics.

2.2. Structural Analysis

An X-ray diffraction (XRD) device (MiniFlex600, Rigaku, Tokyo, Japan) was used to characterize phases of $Yb_{1-x}Al_xTaO_4$. The microstructure, as well as elemental distribution and content, were analyzed using energy-dispersive X-ray energy spectroscopy (EDS, Quantax 200, Bruker, Karlsruhe, Germany) and scanning electron microscopy (SEM, SIGMA-300, ZEISS, Oberkochen, Germany). The actual density (ρ) was obtained by the Archimedes principle:

$$\rho = \frac{m_1}{m_3 - m_2} \quad (1)$$

where m_1 was the initial weight, m_2 was the weight placed in water, and m_3 was the saturated wet weight of the sample.

2.3. Properties Measurements

The TECs (α_p) were measured within a thermal expansion device (DIL 402, NETZSCH, Bavaria, Germany) at 30–1400 °C based on the thermal expansion rate (dL/L_0):

$$\alpha_p = \frac{dL/L_0}{\Delta T} \quad (2)$$

where dL, L_0, and ΔT were elongations in length, original length, and change in temperature, respectively.

The Young's modulus and hardness of $Yb_{1-x}Al_xTaO_4$ were measured using a nano-indentation device (Nanomechanisc, Inc. iMicro, Milpitas, CA, USA) according to the nano-indentation depth (h $\leq$ 0.2 μm) specified in the national standard GB/T21838.1-2008 [37]. The load was 50 mN, and the holding time was 10 s because the nano Young's modulus and hardness were stable when the load was higher than 20 mN in our previous study. A holding time of 10 s was used to stabilize the contact area between the sample and the nano-indenter.

3. Results and Discussion

3.1. Crystal and Microstructure

Figure 1a shows experimental XRD patterns of $Yb_{1-x}Al_xTaO_4$ ceramics compared with the standard ICDD cards. When x is 0.05–0.1, $Yb_{1-x}Al_xTaO_4$ is crystallized into a monoclinic-prime (m') phase, and its corresponding standard card is PDF#24-1416. When x = 0.2–0.5, XRD patterns correspond to the standard card of PDF#24-1413 and 24-1416, indicating that $Yb_{1-x}Al_xTaO_4$ (x = 0.2–0.5) is a mixture of m' and monoclinic (m) phases. Figure 1b shows that the XRD peaks of $Yb_{1-x}Al_xTaO_4$ are obviously shifted to a higher angle with an increment in Al content. The Al^{3+} ion has a shorter ionic radius than Yb^{3+}, and Al^{3+} substitutes Yb^{3+} will contract lattice volumes [37]. The cell parameters and theoretical densities of $Yb_{1-x}Al_xTaO_4$ are obtained from XRD Rietveld refinement and are shown in Figure 2a–f and Table 1. For most samples, the weighting factor (R_{wp}) is less than 15% and the fitting factor (x^2) is less than 3, which indicates a high credibility of lattice parameters [38].

Figure 3 shows the crystal structures of $Yb_{1-x}Al_xTaO_4$ with different space groups. The unit cell of the m' phase has twisted [YbO_8] dodecahedra and [TaO_6] octahedra. Yb and Ta are layered in different planes, and the structure relies on the connection between [YbO_8] dodecahedra when two kinds of polyhedral are periodically continued along the a-axis. The primary distinctions between the m and m' phases are that the oxygen coordination number of Ta atoms in the m phase is 4 and 6 for the m' phase. According to Hazen and Prewitt's theory, the thermal expansion of metallic ions in polyhedron is affected by their oxygen coordination number [39–42]. The higher the coordination number, the lower the TECs. Thus, m-$Yb_{1-x}Al_xO_4$ may have higher TECs than those with the m' phase, and it will be discussed in Section 3.3.

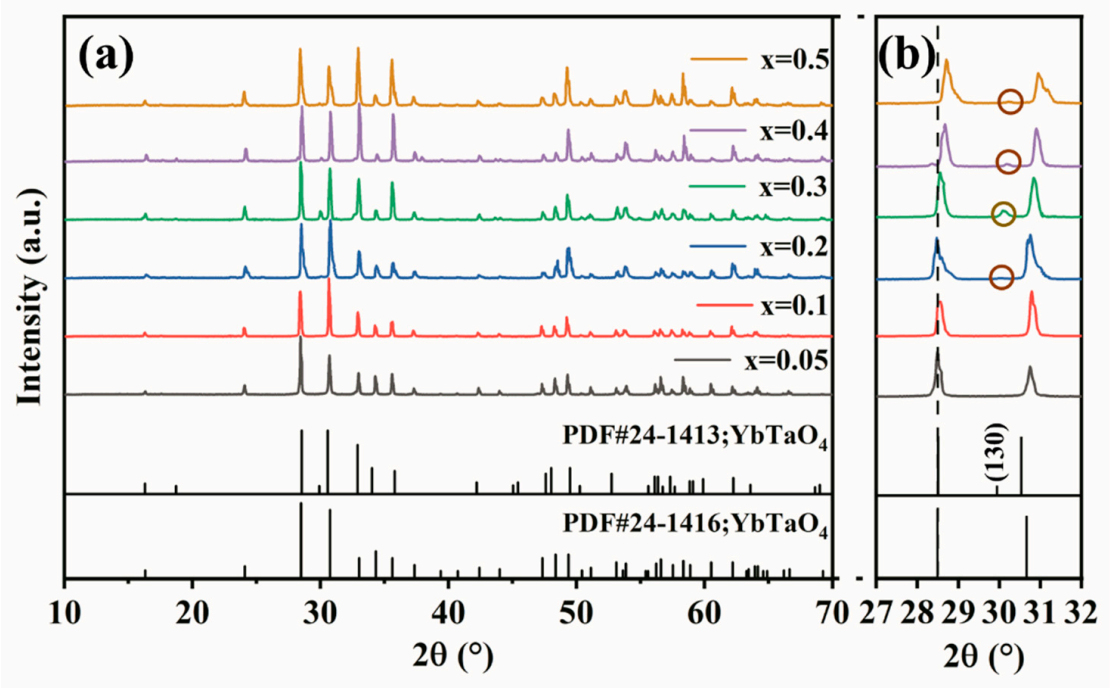


Figure 1. XRD patterns of $Yb_{1-x}Al_xTaO_4$ (x = 0.05, 0.1, 0.2, 0.3, 0.4, 0.5) ceramics; (**a**) XRD patterns compared with standard PDF cards; (**b**) shifts of XRD peaks.

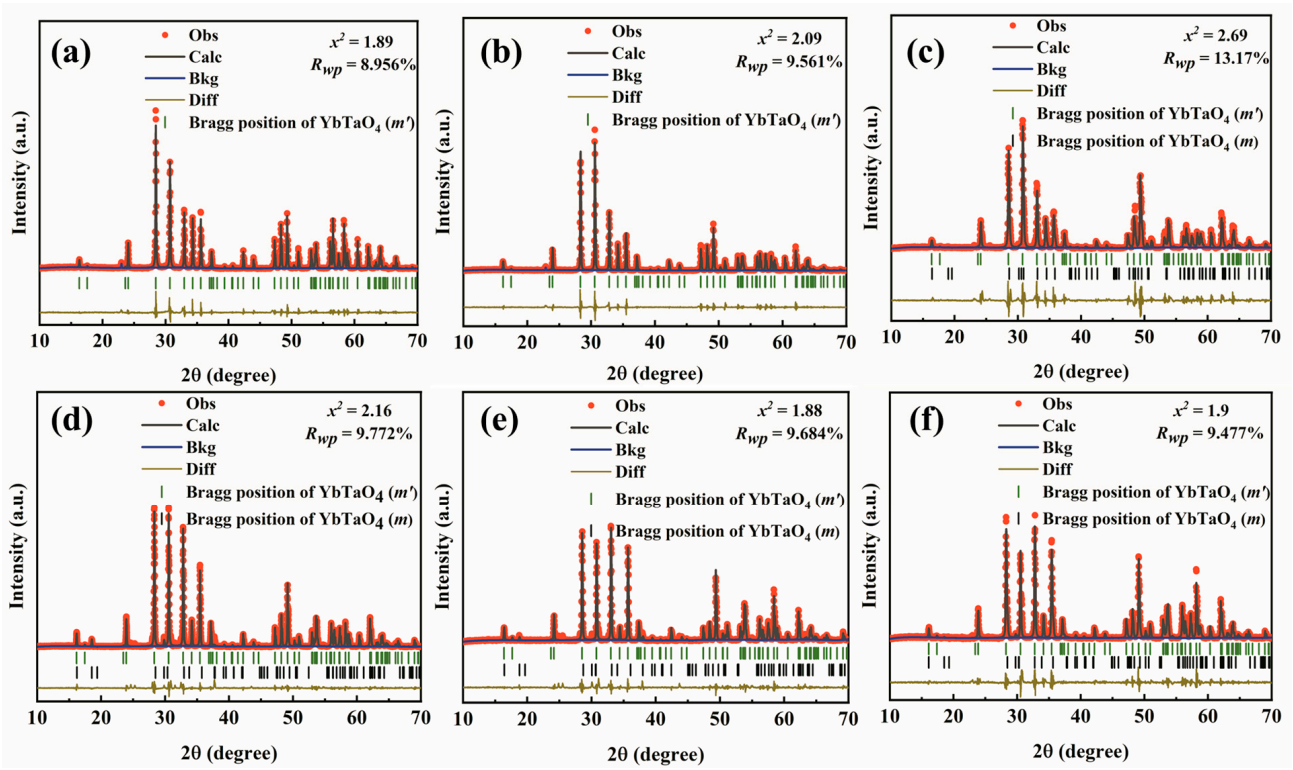


Figure 2. XRD Rietveld refinements of $Yb_{1-x}Al_xTaO_4$ (x = 0.05, 0.1, 0.2, 0.3, 0.4, 0.5) ceramics: (**a**) x = 0.05; (**b**) x = 0.1; (**c**) x = 0.2; (**d**) x = 0.3; (**e**) x = 0.4; (**f**) x = 0.5.

Table 1. Lattice parameters (a, b, c/Å), β angle (β/°), phase content (wt%), unit cell volume (V/Å^3), density (ρ/g·cm^{-3}), and relative density (ρ_R/%) of $Yb_{1-x}Al_xTaO_4$ ceramics.

Samples	Phase	Content	a	b	c	β	V	ρ	ρ_R
0.05	m'	100	5.07	5.26	5.44	96.17	144.192	9.496	97
0.1	m'	100	5.07	5.43	5.26	96.18	144.061	9.357	97
0.2	m'	91.5	5.07	5.43	5.25	96.16	144.005	8.972	98
	m	8.5	6.89	5.27	10.86	133.13	287.507		
0.3	m'	85.5	5.07	5.43	5.25	96.16	143.999	8.650	97
	m	14.5	6.81	5.25	10.89	132.95	285.041		
0.4	m'	80.9	5.07	5.25	5.43	96.18	143.643	8.309	97
	m	19.1	6.86	5.23	10.84	133.03	284.464		
0.5	m'	76.0	5.07	5.25	5.43	96.16	143.518	8.017	96
	m	24.0	6.83	5.19	10.85	132.92	281.963		

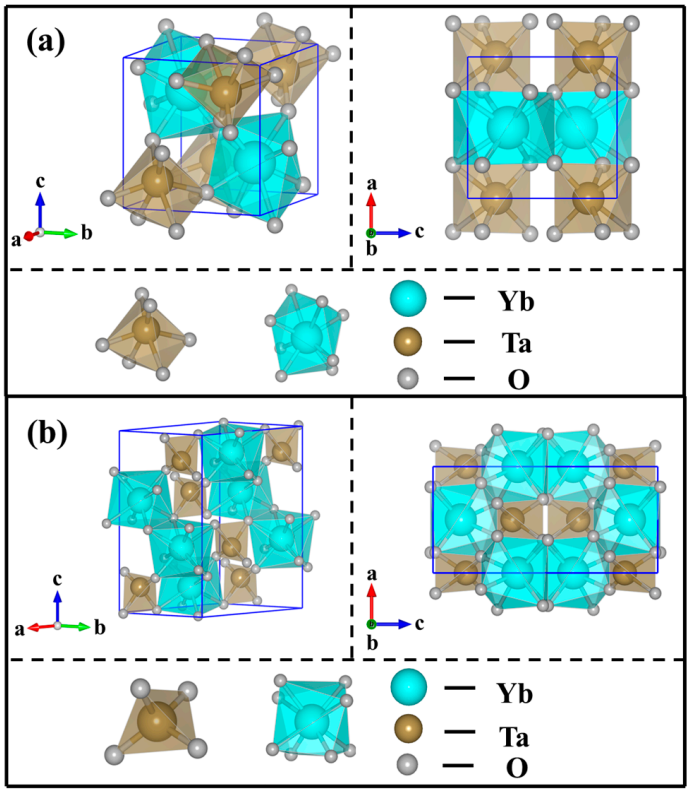


Figure 3. Crystal structures of $Yb_{1-x}Al_xTaO_4$ ceramics with different phases: (**a**) m' phase; (**b**) m phase.

Figure 4a–f shows that the grain sizes of each sample are less than 15 μm. The elemental distribution is analyzed by EDS mapping, and the elemental distribution of $Yb_{1-x}Al_xTaO_4$ is uniform when x = 0.05 and 0.1, while $Yb_{1-x}Al_xTaO_4$ ceramics are two-phase composites when x is greater than 0.1. Figure 4 shows SEM in the backscatter mode, while the differences in color are not obvious because they consist of the same elements. The points marked as 1~8 in Figure 4c–f are measured using an EDS point scan to estimate their elemental content, as shown in Table 2. The Yb content in point 1 is less than that in point 2, and a similar situation is detected in the other three samples. It is believed that segregations of Yb and Al exist in $Yb_{1-x}Al_xTaO_4$ solid solutions; subsequently, this leads to co-formations of m and m' phases. Previous studies prove that lanthanide contraction leads to the m-m' phase transition in $RETaO_4$ ceramics [28,34,39], and Al^{3+} substituting Yb^{3+} reduces the A-site ionic radius in ABO_4-type $YbTaO_4$. The formations of m + m' $Yb_{1-x}Al_xTaO_4$ composites indicate that the solid solubility of Al in $YbTaO_4$ is less than 0.2.

The EDS point scan is semi-quantitative, and it is unable to obtain the accurate chemical forms of *m*- and *m*′-phase $Yb_{1-x}Al_xTaO_4$ ceramics.

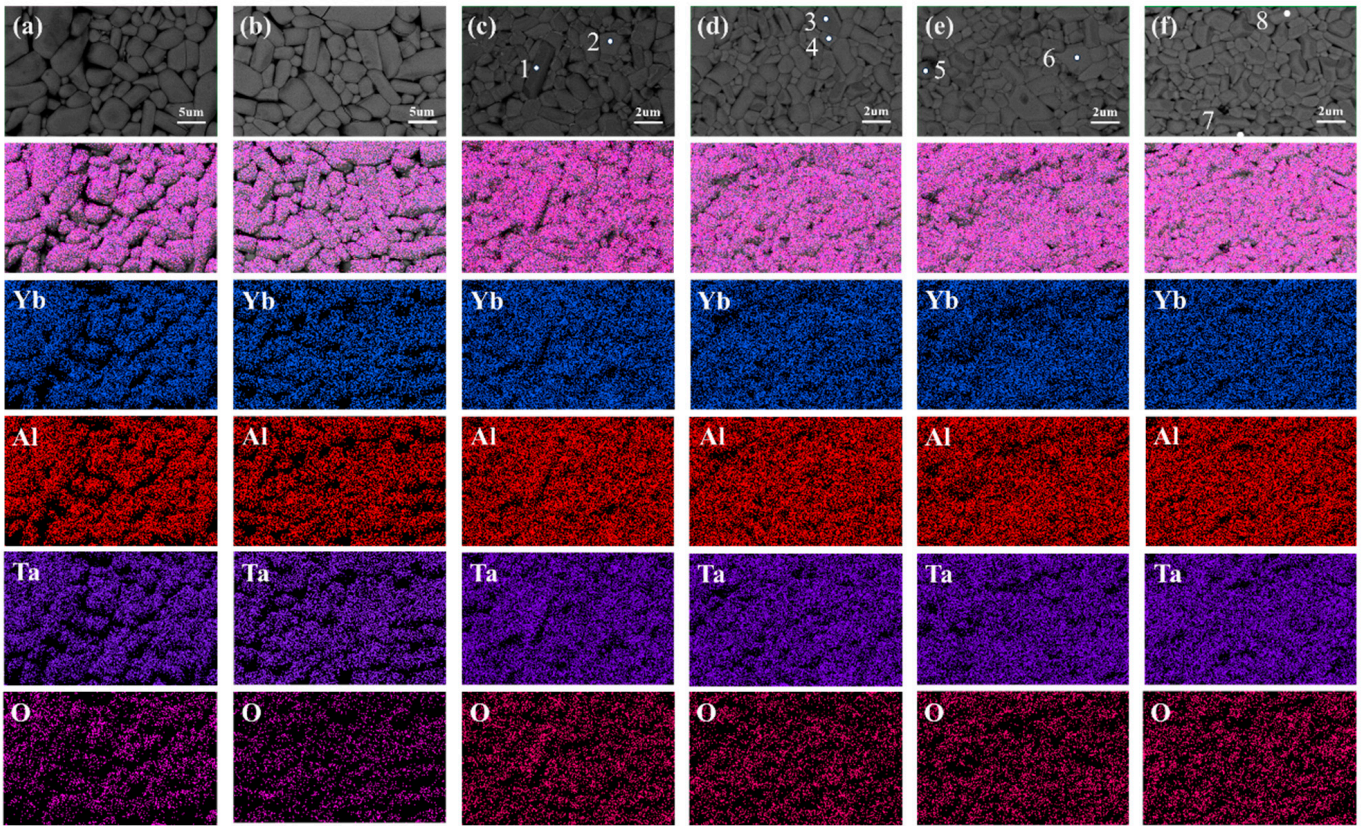


Figure 4. Microstructures and EDS mapping of $Yb_{1-x}Al_xTaO_4$ ceramics: (**a**) x = 0.05; (**b**) x = 0.1; (**c**) x = 0.2; (**d**) x = 0.3; (**e**) x = 0.4; (**f**) x = 0.5.

Table 2. The compositions of $Yb_{1-x}Al_xTaO_4$ (x = 0.2, 0.3, 0.4, 0.5) ceramics, as marked in Figure 4, obtained from an EDS point scan.

Samples	Position	Yb (at%)	Al (at%)	Ta (at%)	O (at%)
$Yb_{0.8}Al_{0.2}TaO_4$	1	3.8	19.73	15.22	61.25
	2	10.95	20.84	19.53	48.68
$Yb_{0.7}Al_{0.3}TaO_4$	3	5.62	20.66	17.98	55.47
	4	9.93	15.75	16.56	57.77
$Yb_{0.6}Al_{0.4}TaO_4$	5	3.86	20.71	17.39	58.04
	6	11.44	17.86	18.66	52.04
$Yb_{0.5}Al_{0.5}TaO_4$	7	3.61	17.30	15.67	63.41
	8	10.39	15.82	17.44	56.35

3.2. Mechanical Properties

Young's modulus is directly related to the bonding strength of crystal [43]. In a practical working environment, turbine engines are subject to impact friction from objects entrained in high-speed airflow. Therefore, a high modulus and high hardness are needed to improve the service life of $YbTaO_4$. Young's modulus (100.9–236.6 GPa) is shown in Figure 5a for $Yb_{1-x}Al_xTaO_4$, which is lower than that of YSZ (250 GPa) but similar to those of $La_2Zr_2O_7$ (237 GPa) and Yb_2SiO_5 (160 GPa) [44–46]. The highest modulus is 236.6 GPa when x = 0.5, and the lowest modulus is 100.9 GPa when x = 0.05. The substitution between Al and Yb increases the bonding strength, which enhances the modulus. Figure 5b shows the hardness (3.7–12.8 GPa) for $Yb_{1-x}Al_xTaO_4$. The highest hardness (12.8 GPa) of

$Yb_{0.5}Al_{0.5}TaO_4$ is higher than other EBC materials, and this phenomenon can be explained by the enhanced bonding strength. When Al substitutes Yb, the Al-O bond is stronger than the Yb-O bond, which increases the bonding strength and hardness. Both $RETaO_4$ and $AlTaO_4$ are monoclinic phases, and $AlTaO_4$ has a far higher bonding strength and modulus than most $RETaO_4$, except $ScTaO_4$. Thus, using Al to substitute Yb can enhance the hardness and modulus of $YbTaO_4$.

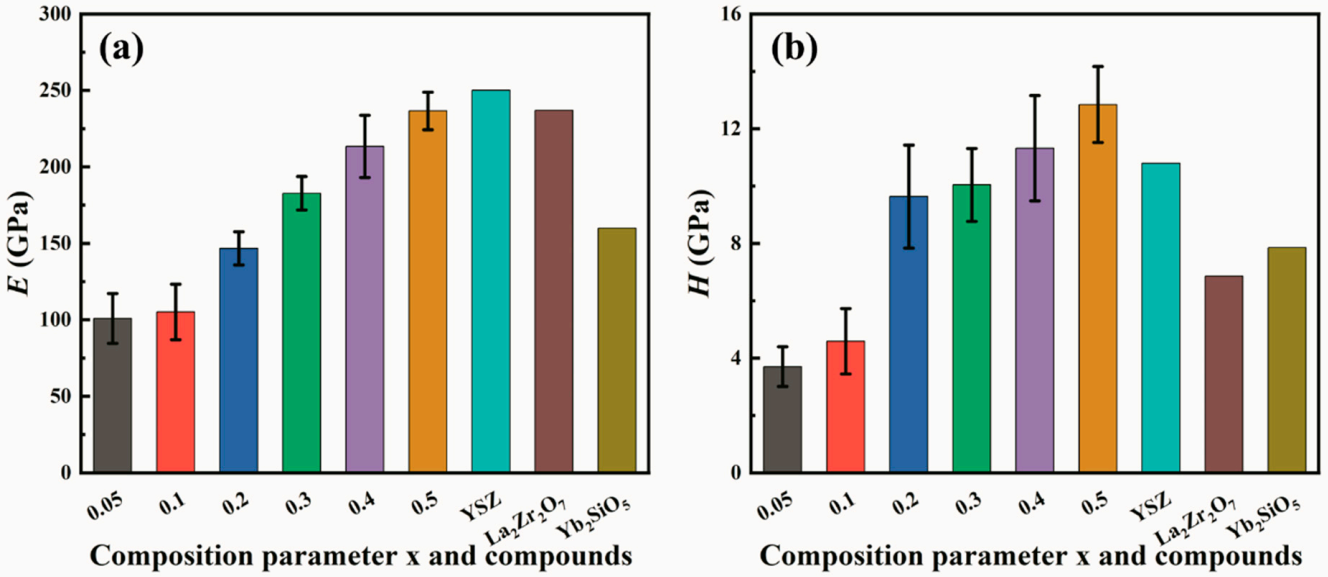


Figure 5. Mechanical properties of $Yb_{1-x}Al_xTaO_4$ (x = 0.05, 0.1, 0.2, 0.3, 0.4, 0.5) and other compounds [44–46]: (**a**) Young's modulus; (**b**) hardness.

3.3. Thermal Expansion Performance

Figure 6a shows the thermal expansion rates of $Yb_{1-x}Al_xTaO_4$, and their slopes are almost constant with the increasing temperature, which can prove their excellent phase stability. Figure 6b shows that the TECs of $Yb_{1-x}Al_xTaO_4$ increase steadily with the increasing temperature, and they are approximately 6.0~9.0 × 10^{-6} K^{-1} at 1400 °C. The TECs of single-phase $Yb_{1-x}Al_xTaO_4$ are lower than that of RE_2SiO_5, while the TECs of bi-phase $Yb_{1-x}Al_xTaO_4$ are similar to or slightly greater than that of RE_2SiO_5 [46]. The TECs of $Yb_{1-x}Al_xTaO_4$ ceramics are similar to those of CMCs, including Al_2O_{3f}/Al_2O_3 (8–9 × 10^{-6} K^{-1}) and SiC_f/SiC (4–6 × 10^{-6} K^{-1}). Indeed, the TECs of $Yb_{0.5}Al_{0.5}TaO_4$ match that of Al_2O_{3f}/Al_2O_3, and the TECs of $Yb_{0.95}Al_{0.05}TaO_4$ match that of SiC_f/SiC. The mathematical expression for TECs is [47]

$$\mathrm{TECs}(T) = \mathrm{TECs}_0(T) + \mathrm{TECs}_1(T) \tag{3}$$

$$\mathrm{TECs}_0(T) = \frac{3k_B}{2\varphi r_0 U}\left(\frac{T}{T_D}\right)^3 g_0(x_D) \tag{4}$$

$$\mathrm{TECs}_1(T) = \frac{3k_B}{2\varphi r_0 U}\frac{k_B T}{2U}\left(\frac{T}{T_D}\right)^3 g_1(x_D) \tag{5}$$

$$g_0(x_D) = \int_0^{\frac{T_D}{T}} \frac{x^4 e^x}{(e^x-1)^2} dx \tag{6}$$

$$g_1(x_D) = \int_0^{\frac{T_D}{T}} \frac{x^5 e^x (1+e^x)}{(e^x-1)^3} dx \tag{7}$$

where φ is the reciprocal of width for the energy barrier, k_B is the Boltzmann's constant, r_0 is the equilibrium inter-ion distance, T_D is the Debye temperature, and U is the crystal-binding

energy. The ionic radius of Al^{3+} is 0.535 Å, and the ionic radius of Yb^{3+} is 0.863 Å. The equilibrium inter-ionic distance decreases with the increasing Al content, and the crystal lattice is more tightly packed. The r_0 is inversely proportional to the TECs; subsequently, the TECs are increased with the increasing Al content. The crystal-binding energy (U) is [48]

$$U = \frac{N_A Az + z - e^2}{r_0}(1 - \frac{1}{B}) \quad (8)$$

where N_A is the Avogadro's constant, A is the Madelung's constant, z is the ionic charge, and B is the Born's index. A decrease in the equilibrium distance causes an increase in the crystal-binding energy which reduces the TECs, which is contrary to the experimental results. The TECs are not determined by a single index since $Yb_{1-x}Al_xTaO_4$ is a composite when x is higher than 0.2. Yang et al. [49] have found that the TECs of m-phase $RETaO_4$ are higher than that of m'-phase $RETaO_4$ because m'-phase $RETaO_4$ has a higher crystal-binding energy. For m-phase $RETaO_4$, the cations and anions are located at two different positions, whereas the cation and anion are located at three different positions in m'-phase $RETaO_4$. The structural differences affect their thermodynamic stability and force constants. The force constant is directly proportional to the bonding strength indicated by the Debye temperature (T_D) [50,51]:

$$T_D = \frac{h}{k_B}\left(\frac{3e}{4\pi V}\right)^{\frac{1}{3}} V_M \quad (9)$$

where e is the total atomic weight per cell and h is the Planck's constant. The Debye temperature is positively correlated with the interatomic bonding force. The strength of the Al-O bond is stronger than that of the Yb-O bond, leading to the Debye temperature being increased. Thus, the TECs of single-phase m'-$Yb_{1-x}Al_xTaO_4$ are reduced with an increasing Al content when x is 0.05~0.2. For x = 0.3~0.5, the TECs of $Yb_{1-x}Al_xTaO_4$ are dramatically increased due to the production of m-$Yb_{1-x}Al_xTaO_4$. Furthermore, thermal expansion is the non-harmonic oscillations of lattices reflected by the Grüneisen parameter (γ):

$$\gamma = \frac{\alpha_p \cdot V \cdot K_T}{C_V} \quad (10)$$

where V is the molar volume, K_T is the isothermal bulk modulus, and C_V is the constant volume heat capacity. Without considering C_V and K_T, the TECs of the m phase are higher than those of the m' phase. Therefore, the Grüneisen parameter of the m phase is larger than that of the m' phase, and a similar situation is reported in $Sm_{1-x}Yb_xTaO_4$ ceramics [39]. There is a theory suggesting that the TECs of metal–oxygen bonds ($TECs_M$) are related to their oxygen coordination number (P) and cation charge (Z) [52–54]:

$$TECs_M = 32.9 \cdot (0.75 - \frac{Z}{P}) \times 10^{-6} \quad (11)$$

Equation (11) expresses that increasing the oxygen coordination number can enhance the TECs when the cation charge is unchanged, indicating that the TECs of Ta-O bonds in $[TaO_4]$ of m-$Yb_{1-x}Al_xTaO_4$ should be lower than that of Ta-O bonds in $[TaO_6]$ of the m' phase. However, a current study of $Yb_{1-x}Sm_xTaO_4$ shows that the m phase has higher TECs than the m' phase attributed to the higher an-harmonic vibrations of lattices. It is believed that crystal structures are the dominators of the TECs for tantalates.

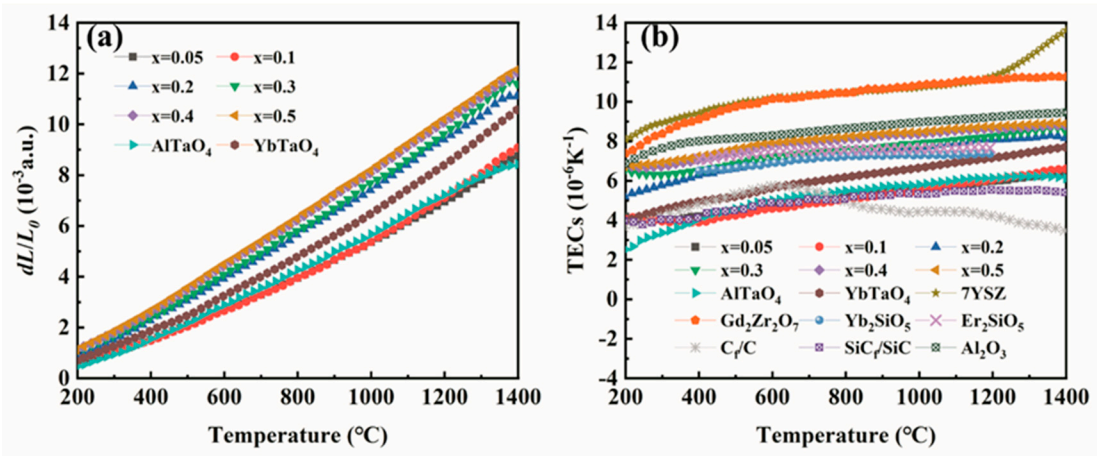


Figure 6. Thermal expansion performance of $Yb_{1-x}Al_xTaO_4$ (x = 0.05, 0.1, 0.2, 0.3, 0.4, 0.5) ceramics [46]: (**a**) thermal expansion rate; (**b**) TECs as a function of temperature.

4. Conclusions

In this study, $Yb_{1-x}Al_xTaO_4$ (x = 0.05, 0.1, 0.2, 0.3, 0.4, 0.5) ceramics are successfully prepared to regulate their properties. The substitution between Al and Yb improves the hardness and modulus because Al-O bonds are stronger than Yb-O bonds. The nano hardness of $Yb_{1-x}Al_xTaO_4$ (x = 0.2, 0.3, 0.4, 0.5) (9.6–12.8 GPa) and the Young's modulus (146.8–236.6 GPa) are increased effectively compared with $YbTaO_4$ and other EBC materials. The TECs of $Yb_{1-x}Al_xTaO_4$ are 6.4–8.9 $\times$ 10^{-6} K^{-1} at 1400 °C, which are similar to those of the Al_2O_3 and SiC matrixes (3–9 $\times$ 10^{-6} K^{-1}). For single-phase m'-$Yb_{1-x}Al_xTaO_4$ (x = 0.05, 0.1), the addition of Al can slightly reduce the TECs because Al-O bonds are stronger than Yb-O bonds, which leads to a decrement in the an-harmonic vibrations of lattices. For bi-phase $Yb_{1-x}Al_xTaO_4$ (x = 0.2–0.5), their TECs increase with the increasing Al content due to the formation of the *m* phase. Crystal structures are the dominators of the TECs for $Yb_{1-x}Al_xTaO_4$ tantalates, which govern their lattice an-harmonic vibrations. Thus, the TECs of $YbTaO_4$ can be regulated by Al substitution. Accompanied with the enhanced mechanical properties, the studied $Yb_{1-x}Al_xTaO_4$ ceramics are promising EBCs.

Author Contributions: Formal analysis, J.L., L.C., L.Z., X.C. and J.F.; Investigation, J.L., L.C., L.Z., X.C., C.X. and T.L.; Writing—original draft, J.L.; Writing—review and editing, L.C. and J.F. All authors have read and agreed to the published version of the manuscript.

Funding: This research was funded by Yunnan Major Scientific and Technological Projects (Grant No. 202302AG050010), General Project in Yunnan Province (Grant No. 202201AT070192 and 202101BE070001-011), and Open Project of Yunnan Precious Metals Laboratory (No. 2023050240).

Institutional Review Board Statement: Not applicable.

Informed Consent Statement: Not applicable.

Data Availability Statement: Data underlying the results presented in this paper are not publicly available at this time due to privacy concerns but may be obtained from the authors upon reasonable request.

Conflicts of Interest: The authors declare no conflicts of interest.

References

1. Vaßen, R.; Jarligo, M.O.; Steinke, T.; Mack, D.E.; Stöver, D. Overview on Advanced Thermal Barrier Coatings. *Surf. Coat. Technol.* **2010**, *205*, 938–942. [CrossRef]
2. Zhao, P. Mechanical Properties, Thermophysical Properties and Electronic Structure of Yb^{3+} or Ce^{4+}-Doped $La_2Zr_2O_7$-Based TBCs. *J. Rare Earths* **2023**, *41*, 588–598. [CrossRef]
3. Wu, Y.; Guo, X.; He, D. Research Progress of CMAS Corrosion and Protection Method for Thermal Barrier Coatings in Aero-engines. *China Surf. Eng.* **2023**, *36*, 1–13.

4. Wang, Y.; Ouyang, J.; Wei, T.; Cao, G.; Liu, Z.; Ding, Z.; Wang, Y.; Wang, Y. Mechanical Properties, Thermal Conductivity and Defect Formation Energies of Samarium Immobilization in $Gd_2Zr_2O_7$: First-Principles Study and Irradiation Experiment. *J. Rare Earths* **2023**, *41*, 422–433. [CrossRef]
5. Ma, Z.; Liu, L.; Zheng, W. Environmental Barrier Coating for Aeroengines: Materials and Properties. *Adv. Ceram.* **2019**, *40*, 331–344.
6. Chen, W.; Duan, H.; Shi, J.-L.; Qian, Y.; Wan, J.; Zhang, X.; Sheng, H.; Guan, B.; Wen, R.; Yin, Y.; et al. Bridging Interparticle Li^+ Conduction in a Soft Ceramic Oxide Electrolyte. *J. Am. Chem. Soc.* **2021**, *143*, 5717–5726. [CrossRef]
7. Liu, L.; Yang, X.; Xiao, G.; Wei, D.; Du, Y. Thermal Performance Affected by the Mesoscopic Characteristics of the Ceramic Matrix Composite for Hypersonic Vehicle. *J. Phys. Conf. Ser.* **2021**, *1786*, 012004.
8. Wang, X.; Gao, X.; Zhang, Z.; Cheng, L.; Ma, H.; Yang, W. Advances in Modifications and High-Temperature Applications of Silicon Carbide Ceramic Matrix Composites in Aerospace: A Focused Review. *J. Eur. Ceram. Soc.* **2021**, *41*, 4671–4688. [CrossRef]
9. Yan, Z.; Peng, H.; Ji, X.; Zhang, D. Preparation of $Yb_2Si_2O_7$ Precursor and Its Agglomerated Powder for Low Pressure Plasma Spraying. *Therm. Spray Technol.* **2022**, *14*, 38–45+22.
10. Kimmel, J.; Miriyala, N.; Price, J.; More, K.; Tortorelli, P.; Eaton, H.; Linsey, G.; Sun, E. Evaluation of CFCC Liners with EBC after Field Testing in a Gas Turbine. *J. Eur. Ceram. Soc.* **2002**, *22*, 2769–2775. [CrossRef]
11. Liu, Y.; Yu, H.; Meng, H.; Chu, Y. Atomic-Level Insights into the Initial Oxidation Mechanism of High-Entropy Diborides by First-Principles Calculations. *J. Mater.* **2024**, *10*, 423–430. [CrossRef]
12. Wen, Z.; Tang, Z.; Liu, Y.; Zhuang, L.; Yu, H.; Chu, Y. Ultrastrong and High Thermal Insulating Porous High-Entropy Ceramics up to 2000 °C. *Adv. Mater.* **2024**, *36*, 2311870. [CrossRef]
13. Du, J.; Liu, R.; Wan, F.; Li, D.; Li, J.; Wang, Y. Failure Mechanism of Ytterbium Silicate/Silicon Bi-Layer Environmental Barrier Coatings on SiC_f/SiC Composites upon Long-Time Water Vapor and Oxygen Corrosion Test. *Surf. Coat. Technol.* **2022**, *447*, 128871. [CrossRef]
14. Yang, F.; Fan, Y.; Zhao, J.; Liu, Y.; Chu, K.; Li, Y.; Li, W.; Liu, B. Mechanical and Thermal Properties for Corrosion Products of Lutetium Silicates against CMAS. *J. Am. Ceram. Soc.* **2024**, *107*, 5285–5297. [CrossRef]
15. Fan, Y.; Bai, Y.; Li, Q.; Lu, Z.; Chen, D.; Liu, Y.; Li, W.; Liu, B. Compositional Design and Phase Formation Capability of High-Entropy Rare-Earth Disilicates from Machine Learning and Decision Fusion. *npj Comput. Mater.* **2024**, *10*, 95. [CrossRef]
16. Richards, B.T.; Sehr, S.; De Franqueville, F.; Begley, M.R.; Wadley, H.N.G. Fracture Mechanisms of Ytterbium Monosilicate Environmental Barrier Coatings during Cyclic Thermal Exposure. *Acta Mater.* **2016**, *103*, 448–460. [CrossRef]
17. Yuan, K.; Hou, W.; Ji, X.; Lu, X. Study on Microstructure Evolution in Ytterbium Silicate Environmental Barrier Coatings under Thermal Shock Tests. *Therm. Spray Technol.* **2023**, *15*, 13–18.
18. Tian, J.; Chen, L.; Chen, X.; Luo, K.; Li, B.; Zhang, D.; Wang, M.; Xu, B.; Ren, Z.; Yan, S.; et al. Regulation of Crystal and Microstructures of $RETaO_4$ (RE = Nd, Sm, Gd, Ho, Er) Powders Synthesized via Co-Precipitation. *J. Rare Earths* 2024, *in press*. [CrossRef]
19. Deijkers, J.A.; Wadley, H.N.G. A Duplex Bond Coat Approach to Environmental Barrier Coating Systems. *Acta Mater.* **2021**, *217*, 117167. [CrossRef]
20. Chen, L.; Li, B.; Guo, J.; Zhu, Y.; Feng, J. High-Entropy Perovskite $RETa_3O_9$ Ceramics for High-Temperature Environmental/Thermal Barrier Coatings. *J. Adv. Ceram.* **2022**, *11*, 556–569. [CrossRef]
21. Turcer, L.R.; Sengupta, A.; Padture, N.P. Low Thermal Conductivity in High-Entropy Rare-Earth Pyrosilicate Solid-Solutions for Thermal Environmental Barrier Coatings. *Scr. Mater.* **2021**, *191*, 40–45. [CrossRef]
22. Federer, J.I. Alumina Base Coatings for Protection of SiC Ceramics. *J. Mater. Eng.* **1990**, *12*, 141–149. [CrossRef]
23. Lee, K.N.; Miller, R.A. Development and Environmental Durability of Mullite and Mullite/YSZ Dual Layer Coatings for SiC and Si_3N_4 Ceramics. *Surf. Coat. Technol.* **1996**, *86–87*, 142–148. [CrossRef]
24. Jiang, C.; Feng, M.; Yu, C.; Bao, Z.; Zhu, S.; Wang, F. Thermal Cycling Behavior of Nanostructured and Conventional Yttria-Stabilized Zirconia Thermal Barrier Coatings via Air Plasma Spray. *Rare Met.* **2023**, *42*, 3859–3869. [CrossRef]
25. Cojocaru, C.V.; Kruger, S.E.; Moreau, C.; Lima, R.S. Elastic Modulus Evolution and Behavior of Si/Mullite/BSAS-Based Environmental Barrier Coatings Exposed to High Temperature in Water Vapor Environment. *J. Therm. Spray Technol.* **2011**, *20*, 92–99. [CrossRef]
26. Chen, P.; Xiao, P.; Li, Z.; Wang, Y.; Tang, X.; Li, Y. Water Vapor Corrosion Behavior and Failure Mechanism of Air Sprayed Bi-Layer $Yb_2Si_2O_7$/SiC and Tri-Layer $Yb_2Si_2O_7$/(SiC_w-Mullite)/SiC Environmental Barrier Coating. *Adv. Powder Mater.* **2023**, *2*, 100064. [CrossRef]
27. Dong, Y.; Ren, K.; Wang, Q.; Shao, G.; Wang, Y. Interaction of Multicomponent Disilicate $(Yb_{0.2}Y_{0.2}Lu_{0.2}Sc_{0.2}Gd_{0.2})_2Si_2O_7$ with Molten Calcia-Magnesia-Aluminosilicate. *J. Adv. Ceram.* **2022**, *11*, 66–74. [CrossRef]
28. Chen, L.; Wang, J.; Li, B.; Luo, K.; Feng, J. Simultaneous Manipulations of Thermal Expansion and Conductivity in Symbiotic $ScTaO_4$/$SmTaO_4$ Composites via Multiscale Effects. *J. Adv. Ceram.* **2023**, *12*, 1625–1640. [CrossRef]
29. Meng, H.; Yu, R.; Tang, Z.; Wen, Z.; Yu, H.; Chu, Y. Formation Ability Descriptors for High-Entropy Diborides Established through High-Throughput Experiments and Machine Learning. *Acta Mater.* **2023**, *256*, 119132. [CrossRef]
30. Gatzen, C.; Mack, D.E.; Guillon, O.; Vaßen, R. $YAlO_3$—A Novel Environmental Barrier Coating for Al_2O_3/Al_2O_3–Ceramic Matrix Composites. *Coatings* **2019**, *9*, 609. [CrossRef]

31. Chen, Z.; Lin, C.; Zheng, W.; Song, X.; Jiang, C.; Niu, Y.; Zeng, Y. Influence of Average Radii of RE^{3+} Ions on Phase Structures and Thermal Expansion Coefficients of High-Entropy Pyrosilicates. *J. Adv. Ceram.* **2023**, *12*, 1090–1104. [CrossRef]
32. Song, C.; Ye, F.; Cheng, L.; Liu, Y.; Zhang, Q. Long-Term Ceramic Matrix Composite for Aeroengine. *J. Adv. Ceram.* **2022**, *11*, 1343–1374. [CrossRef]
33. Chen, L.; Li, B.; Feng, J. Rare-Earth Tantalates for Next-Generation Thermal Barrier Coatings. *Prog. Mater Sci.* **2024**, *144*, 101265. [CrossRef]
34. Chen, L.; Hu, M.; Guo, J.; Chong, X.; Feng, J. Mechanical and Thermal Properties of $RETaO_4$ (RE = Yb, Lu, Sc) Ceramics with Monoclinic-Prime Phase. *J. Mater. Sci. Technol.* **2020**, *52*, 20–28. [CrossRef]
35. Zhang, X.; Li, M.; Zhang, A.; Guo, S.; Mao, J.; Deng, C.; Wang, P.; Deng, C.; Feng, J.; Liu, M.; et al. Al-Modification for PS-PVD 7YSZ TBCs to Improve Particle Erosion and Thermal Cycle Performances. *J. Adv. Ceram.* **2022**, *11*, 1093–1103. [CrossRef]
36. Zhang, J.; Tan, X.; Fan, X.; Mao, J.; Deng, C.-M.; Liu, M.; Zhou, K.; Zhang, X. Thermal Insulation Performance of 7YSZ TBCs Adjusted via Al Modification. *Rare Met.* **2023**, *42*, 994–1004. [CrossRef]
37. Shi, X.; Liu, W.; Li, M.; Sun, Q.; Xu, S.; Du, D.; Zou, J.; Chen, Z. A Solvothermal Synthetic Environmental Design for High-Performance SnSe-Based Thermoelectric Materials. *Adv. Energy Mater.* **2022**, *12*, 2200670. [CrossRef]
38. McCusker, L.B.; Von Dreele, R.B.; Cox, D.E.; Louër, D.; Scardi, P. Rietveld Refinement Guidelines. *J. Appl. Crystallogr.* **1999**, *32*, 36–50. [CrossRef]
39. Chen, L.; Hu, M.; Feng, J. Defect-Dominated Phonon Scattering Processes and Thermal Transports of Ferroelastic $(Sm_{1-X}Yb_X)TaO_4$ Solid Solutions. *Mater. Today Phys.* **2023**, *35*, 101118. [CrossRef]
40. Dolan, M.D.; Harlan, B.; White, J.S.; Hall, M.; Misture, S.T.; Bancheri, S.C.; Bewlay, B. Structures and anisotropic thermal expansion of the α, β, γ, and δ polymorphs of $Y_2Si_2O_7$. *Power Diffr.* **2008**, *23*, 20–25. [CrossRef]
41. Chen, L.; Hu, M.; Zheng, X.; Feng, J. Characteristics of Ferroelastic Domains and Thermal Transport Limits in HfO_2 Alloying $YTaO_4$ Ceramics. *Acta Mater.* **2023**, *251*, 118870. [CrossRef]
42. Kong, F.; Tao, S.; Qian, B.; Gao, L. Facile Synthesis of $MTaO_4$ (M = Al, Cr and Fe) Metal Oxides and Their Application as Anodes for Lithium-Ion Batteries. *Ceram. Int.* **2018**, *44*, 8827–8831. [CrossRef]
43. Nie, G.; Bao, Y.; Wan, D.; Tian, Y. Evaluating High Temperature Elastic Modulus of Ceramic Coatings by Relative Method. *J. Adv. Ceram.* **2017**, *6*, 288–303. [CrossRef]
44. Ren, X.; Pan, W. Mechanical Properties of High-Temperature-Degraded Yttria-Stabilized Zirconia. *Acta Mater.* **2014**, *69*, 397–406. [CrossRef]
45. Liu, B.; Liu, Y.; Zhu, C.; Xiang, H.; Chen, H.; Sun, L.; Gao, Y.; Zhou, Y. Advances on Strategies for Searching for next Generation Thermal Barrier Coating Materials. *J. Mater. Sci. Technol.* **2019**, *35*, 833–851. [CrossRef]
46. Ren, X.; Tian, Z.; Zhang, J.; Wang, J. Equiatomic Quaternary $(Y_{1/4}Ho_{1/4}Er_{1/4}Yb_{1/4})_2SiO_5$ Silicate: A Perspective Multifunctional Thermal and Environmental Barrier Coating Material. *Scr. Mater.* **2019**, *168*, 47–50. [CrossRef]
47. Ruffa, A.R. Temperature Dependence of the Elastic Shear Moduli of the Cubic Metals. *Phys. Rev. B* **1977**, *16*, 2504–2514. [CrossRef]
48. Quane, D. Crystal Lattice Energy and the Madelung Constant. *J. Chem. Educ.* **1970**, *47*, 396. [CrossRef]
49. Yang, K.; Chen, L.; Wu, F.; Zheng, Q.; Li, J.; Song, P.; Wang, Y.; Liu, R.; Feng, J. Thermophysical Properties of $Yb(Ta_xNb_{1-x})O_4$ Ceramics with Different Crystal Structures. *Ceram. Int.* **2020**, *46*, 28451–28458. [CrossRef]
50. Han, Y.; Yu, R.; Liu, H.; Chu, Y. Synthesis of the Superfine High-Entropy Zirconate Nanopowders by Polymerized Complex Method. *J. Adv. Ceram.* **2022**, *11*, 136–144. [CrossRef]
51. Anderson, O.L. A Simplified Method for Calculating the Debye Temperature from Elastic Constants. *J. Phys. Chem. Solids* **1963**, *24*, 909–917. [CrossRef]
52. Hazen, R.M.; Prewitt, C.T. Effects of Temperature and Pressure on Interatomic Distances in Oxygen-Based Minerals. *Am. Mineral.* **1977**, *62*, 309–315.
53. Hazen, R.M. Effects of Temperature and Pressure on the Crystal Structure of Ferromagnesian Olivine. *Am. Mineral.* **1977**, *62*, 286–295.
54. Ridley, M.; Gaskins, J.; Hopkins, P.; Opila, E. Tailoring Thermal Properties of Multi-Component Rare Earth Monosilicates. *Acta Mater.* **2020**, *195*, 698–707. [CrossRef]

Disclaimer/Publisher's Note: The statements, opinions and data contained in all publications are solely those of the individual author(s) and contributor(s) and not of MDPI and/or the editor(s). MDPI and/or the editor(s) disclaim responsibility for any injury to people or property resulting from any ideas, methods, instructions or products referred to in the content.